Article

Hybridization of Co$_3$S$_4$ and Graphitic Carbon Nitride Nanosheets for High-Performance Nonenzymatic Sensing of H$_2$O$_2$

Asha Ramesh [1], Ajay Ajith [2], Neeraja Sinha Gudipati [1], Siva Rama Krishna Vanjari [3], S. Abraham John [2], Vasudevanpillai Biju [4] and Ch Subrahmanyam [1,*]

1   Department of Chemistry, Indian Institute of Technology Hyderabad, Kandi, Sangareddy 502285, Telangana, India
2   Centre for Nanoscience and Nanotechnology, Department of Chemistry, The Gandhigram Rural Institute, Gandhigram, Dindigul 624302, Tamilnadu, India
3   Department of Electrical Engineering, Indian Institute of Technology Hyderabad, Kandi, Sangareddy 502285, Telangana, India
4   Research Institute for Electronic Science, Hokkaido University, Sapporo, Hokkaido 001-0020, Japan
*   Correspondence: csubbu@chy.iith.ac.in

Abstract: The development of efficient H$_2$O$_2$ sensors is crucial because of their multiple functions inside and outside the biological system and the adverse effects that a higher concentration can cause. This work reports a highly sensitive and selective non-enzymatic electrochemical H$_2$O$_2$ sensor achieved through the hybridization of Co$_3$S$_4$ and graphitic carbon nitride nanosheets (GCNNS). The Co$_3$S$_4$ is synthesized via a hydrothermal method, and the bulk g-C$_3$N$_4$ (b-GCN) is prepared by the thermal polycondensation of melamine. The as-prepared b-GCN is exfoliated into nanosheets using solvent exfoliation, and the composite with Co$_3$S$_4$ is formed during nanosheet formation. Compared to the performances of pure components, the hybrid structure demonstrates excellent electroreduction towards H$_2$O$_2$. We investigate the H$_2$O$_2$-sensing performance of the composite by cyclic voltammetry, differential pulse voltammetry, and amperometry. As an amperometric sensor, the Co$_3$S$_4$/GCNNS exhibits high sensitivity over a broad linear range from 10 nM to 1.5 mM H$_2$O$_2$ with a high detection limit of 70 nM and fast response of 3 s. The excellent electrocatalytic properties of the composite strengthen its potential application as a sensor to monitor H$_2$O$_2$ in real samples. The remarkable enhancement of the electrocatalytic activity of the composite for H$_2$O$_2$ reduction is attributed to the synergistic effect between Co$_3$S$_4$ and GCNNS.

Keywords: Co$_3$S$_4$; g-C$_3$N$_4$ nanosheets; H$_2$O$_2$ sensor; cyclic voltammetry; differential pulse voltammetry; amperometry; electrochemical sensor

1. Introduction

H$_2$O$_2$ is an important chemical in many fields, including the biomedical, pharmaceutical, food, and textile industries [1–3]. It is also a reactive oxygen species abundant in living organisms and is essential for maintaining regular biological functions. At normal concentrations, it functions as a signaling molecule for neural development and cell proliferation and is a byproduct of cellular metabolism [4]. However, abnormal levels of H$_2$O$_2$ in a cell cause oxidative stress, leading to aging and diseases such as Parkinson's, Alzheimer's, cardiovascular diseases, cancers, or inflammation, and is, therefore, a biomarker [5,6]. As a result, the accurate and efficient determination of H$_2$O$_2$ is imperative, and the drive to develop inexpensive and highly sensitive H$_2$O$_2$ sensors has increased significantly.

There are different methods to detect H$_2$O$_2$, such as fluorimetry, titrimetry, chemiluminescence, and spectrophotometry [7–10]. However, electrochemical methods offer a better platform for fast, sensitive, inexpensive, and portable sensing [6,11]. For the electrochemical detection of H$_2$O$_2$, enzymatic or non-enzymatic sensors can be used. With enzymatic

sensors, enzymes catalyze the reduction of H_2O_2. Although they have high sensitivity and good selectivity, the enzymatic electrochemical sensors suffer from the instability of the enzymes to various variables such as temperature, pH, etc., and they are expensive and have poor reproducibility [12]. Consequently, the non-enzymatic electrochemical sensing of H_2O_2 becomes of great importance.

The enzyme-free H_2O_2 sensors employ nanostructured and morphologically impressive electroactive materials, including metal oxides, sulfides, and carbon nanomaterials, as modifiers of conventional electrodes [13]. Cobalt-based nanomaterials, especially Co_3O_4, are extensively studied for H_2O_2 detection due to their good catalytic activity and high stability, and they are known to be very active towards H_2O_2 [1,14–18]. Similar in structure to Co_3O_4, Co_3S_4 is another spinel compound with superior electrochemical properties, abundant oxidation states for Faraday processes, and high theoretical specific capacity. It is mainly used for energy storage applications [19,20]. Octahedral and tetrahedral positions are occupied by cobalt in their Co^{3+} and Co^{2+} states, respectively. It is a superior electrocatalyst because the metal–sulfur bond is weaker than oxygen. Substitution with a bigger anion reduces the material's band gap, permitting faster electron transport in Co_3S_4 than in Co_3O_4 [21,22]. However, the potential application of these materials in electrochemical sensing is not well explored, and few recent studies can be found in the literature [22–25]. The only study of Co_3S_4 for H_2O_2 detection was by Chen et al., in which they prepared core–shell $Cu_2S@Co_3S_4$ heterostructures by hydrothermal as an electrocatalyst for H_2O_2 reduction. The superior electrocatalytic performance of the sensor was attributed to the microstructure and the synergistic effect between Co_3S_4 and Cu_2S, where more Co(II) electrocatalytic sites are formed by the transfer of electrons from Cu_2S to Co_3S_4 [24]. However, to be further explored as a sensor, the limitations of Co_3S_4, such as less surface area and lower conductivity, need to be improved. Hybridizing Co_3S_4 with high surface area and highly conductive carbon nanomaterials is one way to do this [2,16].

g-C_3N_4 (GCN) is a π-conjugated polymeric carbon material with a layered structure, and the C and N atoms are sp^2 hybridized. Its structure and surface functionalities give the material good catalytic activity [26]. The bulk g-C_3N_4 (b-GCN) can be synthesized in good yield from low-cost materials. Due to its attractive properties and tunability, it has attracted great interest in electrochemical sensing in recent years [27,28]. The poor electrical conductivity and lower surface area of b-GCN can be significantly improved by tailoring their morphology by converting them into nanosheets. The thermal or solvent exfoliation of b-GCN yields nanosheets with high surface area and high electrical conductivity [26,29]. Ajay et al. compared the electrochemical performance of GCN nanosheets (GCNNS) prepared by solvent and thermal exfoliation and reported the superior electrocatalytic activity of solvent-exfoliated nanosheets [30]. Coupling an electroactive material with GCNNS has proven to be an excellent way to improve sensor performance [3]. In this aspect, Liu et al. integrated ZnO into the GCN matrix to form a highly sensitive H_2O_2 sensor. The performance enhancement of the composite resulted from increases in effective surface area and conductivity [31]. Later Atacan et al. hybridized CuO and GCN to achieve improved electrooxidation of H_2O_2 [32]. Ye et al. developed spherical $ZnFe_2O_4$/GCN nano-micro composites for highly efficient H_2O_2 sensors. The internal synergy between $ZnFe_2O_4$ and GCN promotes conductivity and improves the reaction kinetics at the electrode surface [3]. These studies emphasize the need for detailed investigations of metal oxides or sulfides hybridized with GCN as electrode materials to enhance H_2O_2 sensing.

In the present work, a composite is developed through hybridization between Co_3S_4 and GCNNS to obtain a highly sensitive and selective H_2O_2 sensor that works in a wide range of analyte concentrations and has a detection limit of 70 nM. Co_3S_4 micro flowers were synthesized by a facile hydrothermal method, b-GCN by thermal polycondensation of melamine, and the GCNNS and composite were prepared by solvent exfoliation. The electrocatalytic reduction of H_2O_2 was evaluated using cyclic voltammetry (CV), differential pulse voltammetry (DPV), and amperometry. As shown by impedance spectroscopy, the Co_3S_4/GCNNS showed a lower charge transfer resistance than its counterparts, indicating

the increased electron transfer kinetics at the composite electrode due to the collective effect between Co_3S_4 and GCNNS. The practical application of the developed sensor was evaluated by estimating H_2O_2 in the human serum.

2. Experimental Section

2.1. Synthesis

2.1.1. Co_3S_4

Co_3S_4 micro flowers were synthesized by hydrothermal route [33]. First, 6 mmol of cobalt (II) nitrate hexahydrate was dissolved in 60 mL of distilled water. After stirring for 10 min, 8 mmol of thiourea was added and vigorously stirred for another 15 min. Then, 4 mL of ethylenediamine was added to the above solution, and the color of the solution changed to brown. The solution was transferred to a 100 mL Teflon-lined autoclave and held at 200 °C for 12 h. After that, the reaction mixture was cooled to room temperature. A black-colored product was obtained, which was washed three times with distilled water and ethanol. The product was dried at 60 °C overnight.

2.1.2. GCNNS

b-GCN was synthesized via the thermal polycondensation of melamine. 4 g of melamine was heated at 600 °C in a crucible for 2 h at 25 °C min^{-1} to obtain a yellow-colored b-GCN. The nanosheets were prepared by the solvent exfoliation of b-GCN. 10 mg of b-GCN was dispersed in 10 mL of distilled water and sonicated at 40 kHz for 2 h to obtain the nanosheets [30].

2.1.3. Co_3S_4/GCNNS

First, 10 mg b-GCN was dispersed in 10 mL of distilled water and sonicated for 2 h at 40 kHz to obtain the nanosheets. Then, 2 mg of Co_3S_4 was added to the above dispersion and was further sonicated for 45 min to obtain the Co_3S_4/GCNNS [34,35].

2.2. Fabrication of the Electrodes

The glassy carbon electrode (GCE) was polished with 0.3 and 0.05 μm alumina slurry using a polishing cloth, sonicated for 3 min in distilled water and dried at room temperature. Drop-casting is a simple, efficient, and fast method to modify electrode surfaces [36]. 10 μL of the prepared composite was drop-cast onto the mirror-polished GCE and dried overnight at room temperature. The fabricated Co_3S_4/GCNNS-modified electrode was washed with distilled water and used for electrochemical studies. GCNNS-modified GCE and Co_3S_4-modified GCE were prepared by a similar procedure. A scheme for synthesizing the materials and the fabrication of Co_3S_4/GCNNS is shown in Figure 1.

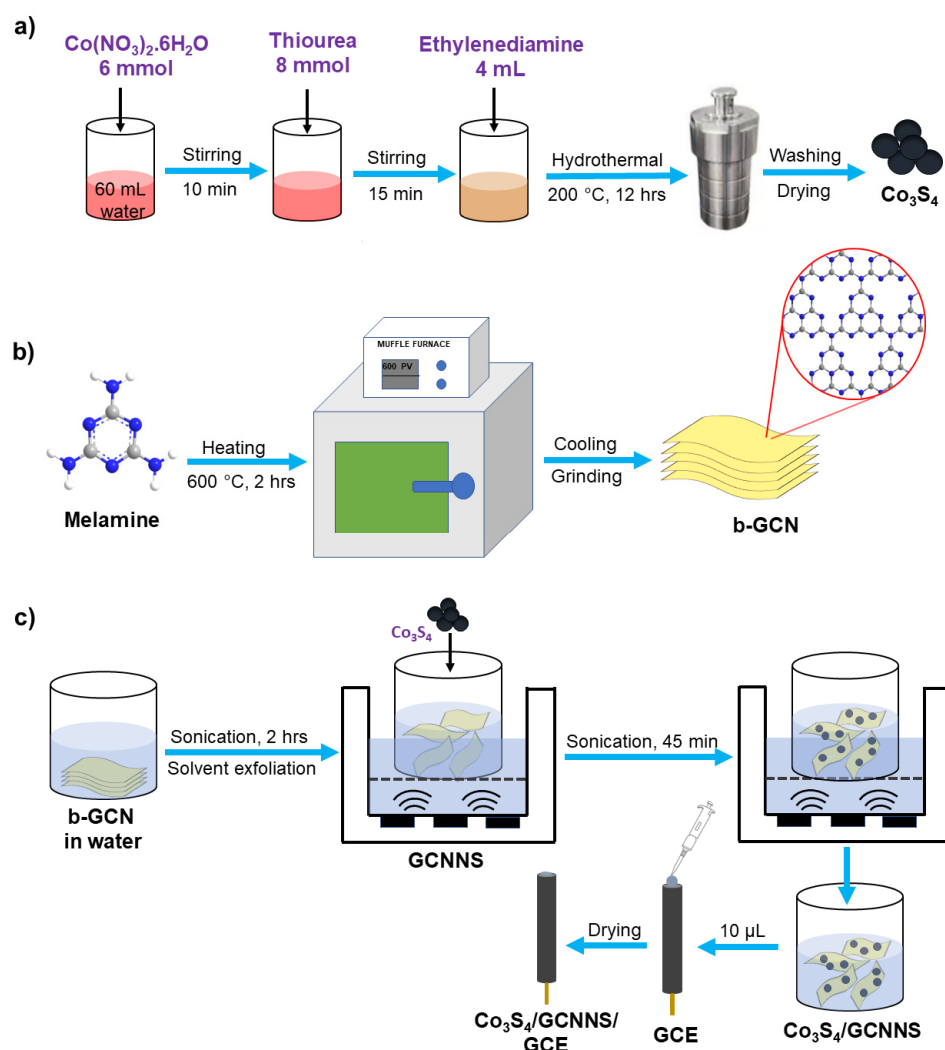**Figure 1.** A scheme for (**a**) hydrothermal synthesis of Co_3S_4, (**b**) synthesis of b-GCN, and (**c**) preparation of Co_3S_4/GCNNS and fabrication of the electrode.

3. Results and Discussion

3.1. Characterization

3.1.1. Crystallographic Studies

Powder X-ray diffraction (XRD) studies of the as-prepared Co_3S_4, b-GCN, GCNNS, and Co_3S_4/GCNNS (Figure 2) help reveal the crystal and phase structure of the prepared materials. The XRD spectra of b-GCN and GCNNS are identical, and the characteristic peaks exist at 2θ values of 12.87° and 27.58° due to diffraction from (100) and (002) crystallographic plane and agree well with the standard JCPDS card no# 87-1526. The peak centered at 12.87° is a feature of the repeating tris triazine structural motifs present in b-GCN and GCNNS, and the peak at 27.58° ascribes to the periodic stacking of layers along the c-axis. The XRD spectrum of Co_3S_4 shows a cubic phase with the diffraction peaks at 2θ values of 31.1°, 36.04°, 47.13°, and 55.0° corresponding to the crystal planes of (311), (400), (422), and (440) aligning well with standard JCPDS card no# 42-1448. As depicted in Figure 2, the XRD pattern of the Co_3S_4/GCNNS nanocomposite shows the presence of both GCNNS and Co_3S_4, ensuring the successful formation of the composite. XRD analysis validated the synthesis of the materials, crystalline behavior, and phase purity.
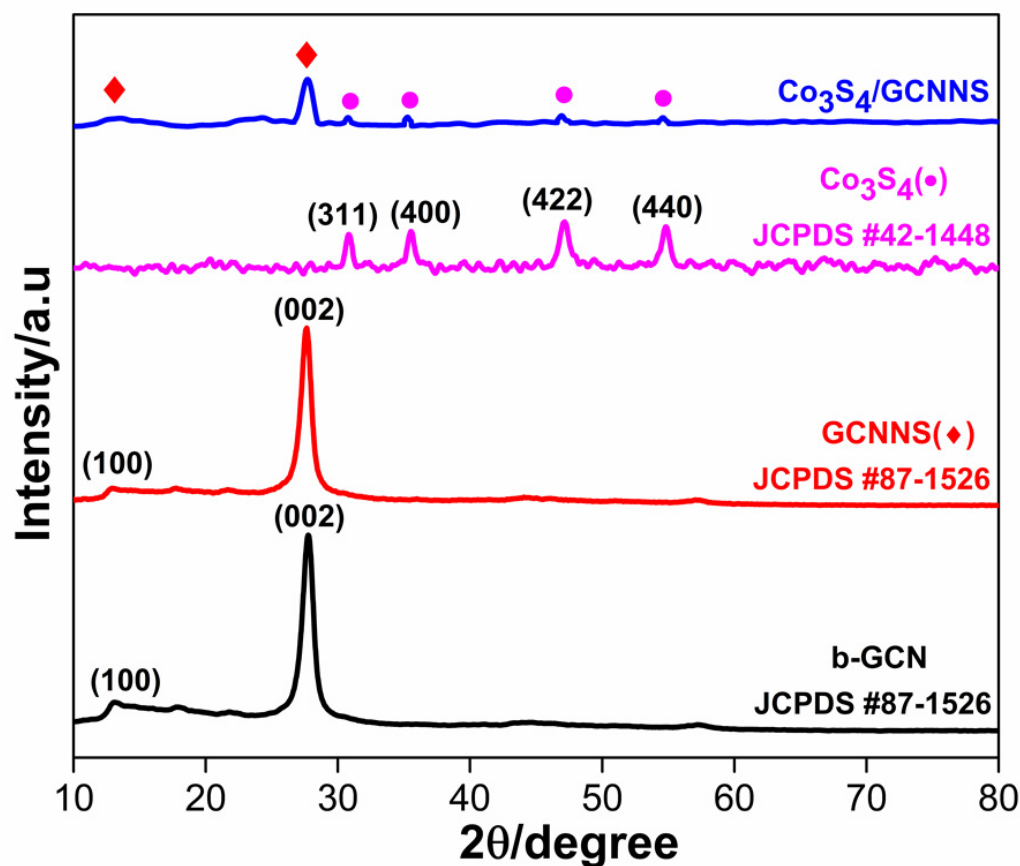
Figure 2. XRD data of b-GCN, GCNNS, Co_3S_4, and Co_3S_4/GCNNS.

3.1.2. XPS Analysis

XPS studies were performed to acquire information about the chemical states of the elements in Co_3S_4, b-GCN, GCNNS, and Co_3S_4/GCNNS. The C/N atomic ratio in the b-GCN was determined to be 0.77, with the atomic percentages of C 1s and N 1s being 44.6 and 55.4, respectively. This confirms the graphitic nature of the prepared b-GCN as it contains C and N in a nearly 3:4 ratio [37,38]. The spectra of Co_3S_4/GCNNS are shown in Figure 3, and those of GCNNS and Co_3S_4 are in Figure S1 (Supplementary Materials). The full-scan spectrum of Co_3S_4/GCNNS in Figure 3a reveals the presence of C, N, Co, and S in the composite. The O detected is due to the oxidation or absorption of oxygen by the sample in the air [39]. As shown in Figure 3b, the high-resolution spectra of C 1s can be deconvoluted into two peaks at 284.8 and 288.0 eV. The peak at 284.8 eV is attributed to graphitic or amorphous carbon present in GCNNS or adsorbed on the surface. The carbon atoms in the $N = C - (N)_2$ group in GCNNS yield a peak at 288.0 eV [35,40]. The high-resolution spectrum of N 1s (Figure 3c) combines four peaks at 398.4, 399.3, 400.5, and 404.6 eV. The peak at 398.4 eV is the N sp^2 bond in $C - N = C$ in the triazine ring, and the peaks at 399.3 and 400.5 eV correspond to the tertiary nitrogen group $(N - (C)_3)$ and the quaternary N three-carbon atom amino functional group $(N - H)$ in the aromatic ring, respectively. The peak at 404.6 eV corresponds to the π excitation of $C = N$ in GCNNS [41].
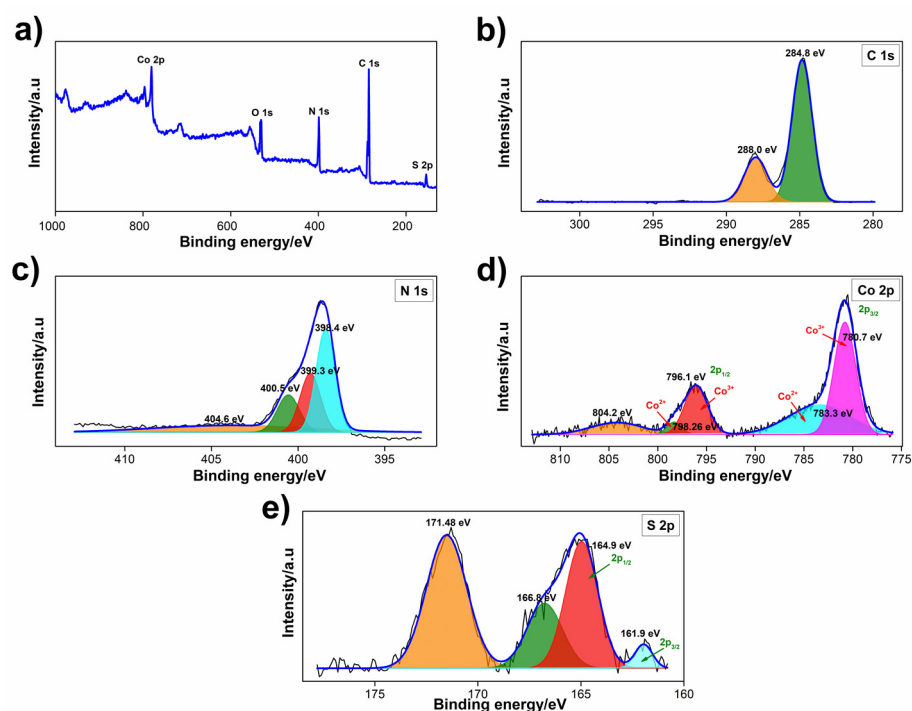
Figure 3. XPS spectra of Co_3S_4/GCNNS (**a**) survey scan, and high-resolution spectra of (**b**) C 1s, (**c**) N 1s, (**d**) Co 2p, (**e**) S 2p.

The high-resolution spectra of Co 2p in the composite (Figure 3d) can be deconvoluted into two spin-orbit doublets of Co^{2+} and Co^{3+}. The peaks 14.96 eV apart at 783.3 and 798.26 eV correspond to the $2p^{3/2}$ and $2p^{1/2}$ orbitals of Co^{2+} in Co_3S_4. Whereas the $2p^{3/2}$ and $2p^{1/2}$ doublet of Co^{3+} appears at 780.7 and 796.1 eV with a spacing of 15.4 eV, suggesting the existence of Co in the +2 and +3 oxidation states in Co_3S_4/GCNNS and a satellite peak appears at 804.2 eV [42,43]. The S 2p spectra (Figure 3e) of Co_3S_4/GCNNS are fitted into four peaks, the peaks at 161.9 and 164.9 eV are indexed to S $2p^{3/2}$ and S $2p^{1/2}$ of S in Co_3S_4 and the two peaks at 166.8 and 171.48 eV belong to S in SO_3^{2-} and SO_4^{2-}, respectively [41]. The results demonstrate the successful formation of the Co_3S_4/GCNNS composite. As shown in Figure S1a, the survey scan of GCNNS showed the presence of C 1s and N 1s, while Co_3S_4 showed the presence of Co 2p and S 2p, and the deconvoluted spectra are shown in Figure S1b,c,e,f. The spectral peaks of the materials are presented in Table S1 for comparison. Interestingly, the binding energy of Co 2p has increased in the composite compared to pure Co_3S_4, and the binding energy of C 1s has decreased compared to its pure counterpart, strongly suggesting the electron transfer between Co_3S_4 and GCNNS in the composite. The decrease in electron density of Co_3S_4 in the composite causes an increase in its binding energy, attributed to the transfer of electrons from Co_3S_4 to GCNNS in the hybrid structure. Meanwhile, the electronegativity of Co (1.88) is lower than that of C and N, further proving that the electron of Co_3S_4 tends to donate to GCNNS. These results prove that the integration between Co_3S_4 and GCNNS in the composite is not just a physical mixture but that there is heterojunction formation with strong electronic interactions [44].

3.1.3. UV-Visible

The UV-visible spectra of Co_3S_4, GCNNS, and Co_3S_4/GCNNS are shown in Figure 4. GCNNS shows a characteristic absorption band at 318 nm due to the π-π* transition in GCNNS, as previously reported [30]. The corresponding absorption in Co_3S_4/GCNNS appears at 321 nm, although the intensity of the absorption has diminished. The slight wavelength shift and decrease in adsorption intensity are attributed to composite formation. Co_3S_4 displays a broad absorption in the 400–800 nm region. Due to the integration of

Co_3S_4 into the GCNNS matrix, the Co_3S_4/GCNNS exhibits greater absorption in the visible light region than that of GCNNS.

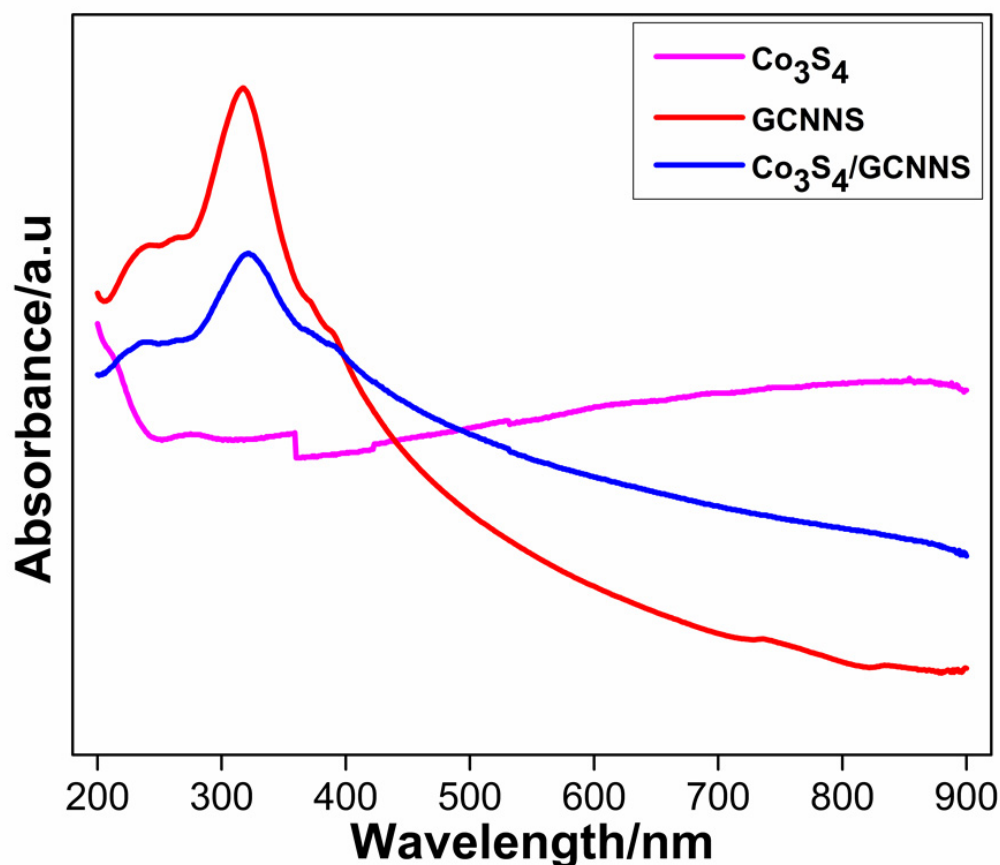**Figure 4.** UV-visible absorption spectra of Co_3S_4, GCNNS and Co_3S_4/GCNNS.

3.1.4. SEM and EDS

The morphology of the synthesized materials was examined by SEM and is shown in Figure 5. The SEM micrograph of the b-GCN shown in Figure 5a is a highly aggregated structure. Further GCNNS was drop-cast and dried on a glassy carbon (GC) plate to record the SEM images (Figure 5b). Interestingly, wrinkled layers with a few-nanometer thicknesses are observed, confirming the formation of the nanosheets. The recorded SEM micrographs of Co_3S_4 (Figure 5c) show a micron-sized flower-like morphology consistent with the literature [33]. Co_3S_4 micro flowers sonicated in water were drop-cast, dried on a GC plate, and examined by SEM to understand whether structural distortion occurs under sonication. No morphological changes were observed. Furthermore, the Co_3S_4/GCNNS modified on the GC plate was analyzed, and as shown in Figure 5d, the composite showed both GCNNS and Co_3S_4 micro flowers, with Co_3S_4 embedded on the GCNNS surface. The Co_3S_4 and GCNNS retain their structure in the composite; however, slight agglomeration was observed in the composite. The elemental composition of the materials was analyzed using EDS. As shown in Figure 5e, the EDS spectrum of Co_3S_4/GCNNS showed the presence of C, N, Co, and S, confirming the formation of the composite. The respective atomic and weight percentages of the elements are presented in Figure 5f. The uniform distribution of the elements can be understood from the elemental mapping shown in Figure 5g.
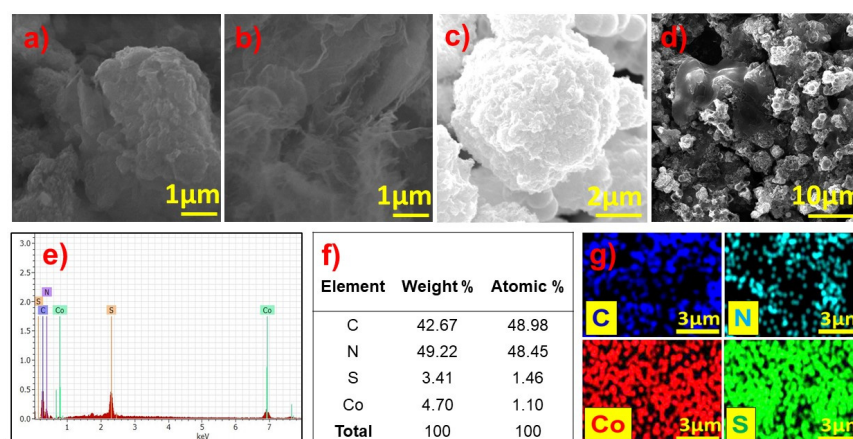
Figure 5. SEM images of (**a**) b-GCN, (**b**) GCNNS, (**c**) Co_3S_4, (**d**) Co_3S_4/GCNNS and (**e**) EDS spectrum of Co_3S_4/GCNNS, (**f**) elemental percentages in Co_3S_4/GCNNS and, (**g**) elemental maps of Co_3S_4/GCNNS.

3.1.5. TEM

TEM images of GCNNS and Co_3S_4/GCNNS were acquired to examine the structure of the materials in detail, and the results are displayed in Figure 6. As shown in Figure 6a, GCNNS consists of very thin, wrinkled nanosheets. The lack of transparency observed in some regions is due to the presence of multilayers. TEM images of Co_3S_4/GCNNS acquired at different magnifications are shown in Figure 6b,c. It is observed that sphere-shaped Co_3S_4 are attached to the surface of GCNNS nanosheets and confirm the formation of the composite. Figure 6e,f show the high-resolution TEM (HRTEM) images captured from the Co_3S_4/GCNNS composite; the fringes with d spacing values of 0.28 nm, 0.23 nm, 0.19 nm, and 0.16 nm can be ascribed to the (311), (400), (422), and (440) crystallographic planes of Co_3S_4 (JCPDS card no# 42-1448). The GCNNS fringes with d spacing values of 0.68 nm and 0.34 nm correspond to the (100) and (002) planes (JCPDS card no# 87-1526). It can be observed that the Co_3S_4 fringes are closely surrounded by GCNNS fringes in the composite, indicating the strong interfacial contact between the materials, which is favorable for the faster electron transfer to promote the electrocatalytic reduction of H_2O_2. As shown in Figure 6d, the SAED pattern of Co_3S_4/GCNNS has a concentric ring structure, revealing the polycrystalline nature of the composite. TEM analysis confirms the successful coupling of GCNNS and Co_3S_4 in the composite.
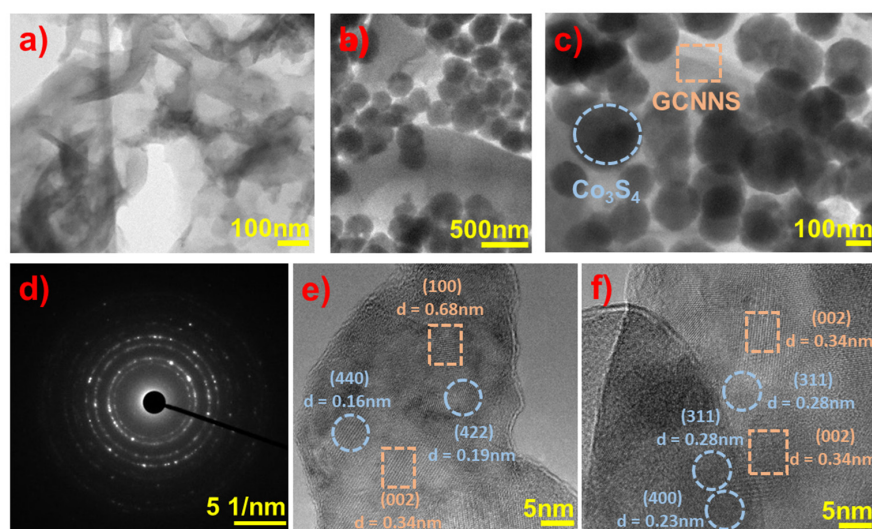

Figure 6. TEM images of (**a**) GCNNS, (**b,c**) Co_3S_4/GCNNS, (**d**) SAED pattern of Co_3S_4/GCNNS, (**e,f**) HRTEM images of Co_3S_4/GCNNS.

3.2. Electrochemical Characterization of Modified Electrodes

3.2.1. Response of Co_3S_4 and Co_3S_4/GCNNS Modified GCE Electrode in NaOH

The formation of the Co_3S_4 and Co_3S_4/GCNNS layer on the GCE surface was examined by recording cyclic voltammograms of the modified electrodes in 0.1 M NaOH at different scan rates of 10–100 mV/s and is shown in Figures 7a,b, respectively. The cyclic voltammograms of Co_3S_4 show four characteristic peaks, including two anodic peaks at 0.22, and 0.50 V and two cathodic peaks at 0.20 and 0.51 V, as shown in Figure 6a, and are consistent with the literature [15,45]. As the scan rate increases, the peak currents increase. These peaks arise from reversible electrochemical redox reactions of cobalt in different oxidation states in the Co_3S_4. Although the mechanisms of these reactions in Co_3S_4 are not well understood, they are expected to be similar to the well-reported redox reactions of $Co(OH)_2$ since the CV profile is similar. There is only a slight deviation in the anodic and cathodic peak potentials of Co_3S_4 from that of $Co(OH)_2$. Oxygen and sulfur also belong to the same group [46]. Furthermore, GCE modified with Co_3S_4/GCNNS (0.2 mg/mL) was characterized in the same way, as illustrated in Figure 6b. The corresponding anodic peak observed in Co_3S_4 can also be seen in the composite in the positive potential scan, and there is an increase in the peak currents, and the peak at 0.22 V becomes prominent. During the negative potential scan, two cathodic peaks corresponding to that in the pure Co_3S_4 are visible, and the reduction peak currents have increased. The results confirm the presence of cobalt in both Co_3S_4 and Co_3S_4/GCNNS electrodes and suggest an improvement in the redox activity of the Co_3S_4 by the composite formation with GCNNS.
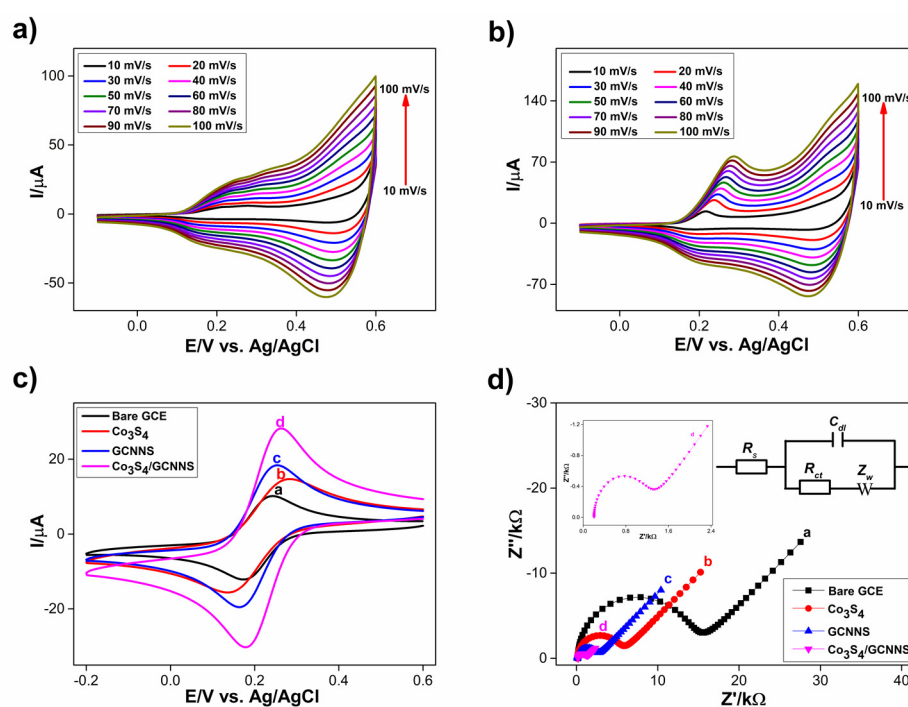

Figure 7. CVs obtained for the response of electrode in 0.1 M NaOH at different scan rates from 10–100 mV s^{-1} (**a**) at the Co_3S_4, (**b**) at the Co_3S_4/GCNNS, (**c**) CVs obtained for the response of modified electrodes in $K_4[Fe(CN)_6]$/$K_3[Fe(CN)_6]$ and (**d**) Nyquist plots of electrodes obtained in $K_4[Fe(CN)_6]$/$K_3[Fe(CN)_6]$ at (**a**) bare GCE (**b**) Co_3S_4, (**c**) GCNNS and (**d**) Co_3S_4/GCNNS-modified GCEs.

3.2.2. $K_4[Fe(CN)_6]$/$K_3[Fe(CN)_6]$ Response of Modified Electrodes and Electroactive Surface Area (EAS)

The electrochemical behavior of bare GCE, Co_3S_4, GCNNS, and Co_3S_4/GCNNS-modified GCE was investigated with $K_4[Fe(CN)_6]$ and $K_3[Fe(CN)_6]$ redox probes. Cyclic voltammograms of the modified electrodes were recorded in 0.1 M KCl containing 1 mM of $K_4[Fe(CN)_6]$/$K_3[Fe(CN)_6]$ each, from a potential range of 0.6 to −0.2 V vs. Ag/AgCl at a

scan rate of 50mV/s and are shown in Figure 7c. A well-defined reversible redox peak for the $K_4[Fe(CN)_6]/K_3[Fe(CN)_6]$ system is observed. Bare GCE showed an oxidation peak current of 10.2 µA, and the redox peaks are separated by 67 mV (ΔE_p). The oxidation peak current was increased when GCE was modified with Co_3S_4 to a value of 14.88 µA, although the ΔEp value has increased to 140 mV. Meanwhile, the GCNNS-modified electrode yielded an oxidation current of 18.57 µA, 1.25 times higher than Co_3S_4, and displayed a peak separation of 90 mV lower than for Co_3S_4. The increase in the response of GCNNS to Fe^{2+}/Fe^{3+} is because the nanosheet morphology of GCNNS favors electron transfer between the analyte and the electrode. These results illustrate the superior electrocatalytic activity of GCNNS towards the Fe^{2+}/Fe^{3+} couple compared to Co_3S_4. The Co_3S_4/GCNNS-modified GCE showed a maximum peak current of 28.20 µA, 1.89 and 1.51 times higher than Co_3S_4 and GCNNS with a ΔEp of 82 mV. Interestingly, the hybridization of Co_3S_4 with GCNNS resulted in a significant increase in the oxidation peak current and a reduced ΔEp compared to its counterparts, strongly indicating the enhanced electrocatalytic aspects and the importance of the synergistic effects of the composite. The electroactive surface area (EAS) of the fabricated electrodes was calculated using the Randles–Sevcik Equation (1),

$$I_p = 2.69 \times 10^5 n^{3/2} A D^{1/2} C \nu^{1/2} \tag{1}$$

where I_p is the peak current at the respective electrode, n is the number of electrons involved (1 for $[Fe(CN)_6]^{3-/4-}$), A is the EAS of the electrode in cm^2, D is the diffusion coefficient (6.7×10^6 cm^2/s), C is the concentration of the redox couple (1 mM), and ν is the scan rate (50 mV/s). The EAS of GCE, Co_3S_4, GCNNS, and Co_3S_4/GCNNS-modified GCE was estimated to be 0.067, 0.097, 0.12, and 0.18 cm^2, respectively. The Co_3S_4/GCNNS-modified GCE has the highest EAS, 1.9 times higher than Co_3S_4 and 1.5 times higher than GCNNS which gives the composite electrode high electrocatalytic activity compared to their pure counterparts.

3.2.3. Electrochemical Impedance Studies

The impedance changes occurring at the electrode surface were further investigated using electrochemical impedance spectroscopy. Nyquist plots of bare GCE, Co_3S_4, GCNNS, and Co_3S_4/GCNNS-modified GCE electrodes were recorded in 0.1 M KCl containing 1 mM $K_4[Fe(CN)_6]/K_3[Fe(CN)_6]$, and the obtained plots are shown in Figure 7d. The impedance data were simulated using the Randles equivalent circuit model and are shown in Figure 7d (inset), where R_S is the ohmic resistance of the electrolyte, R_{CT} is the charge transfer resistance, C_{dl} is the double layer capacitance, and Z_W is the Warburg impedance. The semi-circular region in the Nyquist plots corresponds to the electron transfer limited process, and the diameter is equal to the R_{CT}. The R_{CT} values of the electrodes were determined to be 15.80, 6.28, 2.88, and 1.40 kΩ for bare, Co_3S_4, GCNNS, and Co_3S_4/GCNNS modified GCEs, respectively. When modified with Co_3S_4 or GCNNS, the R_{CT} values become lower than bare GCE values. Meanwhile, Co_3S_4/GCNNS has the lowest R_{CT} value, demonstrating fast electron transfer mediated by the composite, compared to the pure counterparts. The heterogeneous electron transfer rate constant (k_{et}) of $K_4[Fe(CN)_6]/K_3[Fe(CN)_6]$ at the modified electrode is calculated using Equation (2),

$$k_{et} = RT/n^2F^2AR_{CT}C^0 \tag{2}$$

where R is the gas constant (8.314 J.mol^{-1}.K^{-1}), T is the temperature (298 K), n is the number of electrons transferred per molecules of the redox probe (n = 1 for the $[Fe(CN)_6]^{3-/4-}$), F is the Faraday constant (96,485 C), A is the area of the electrode (0.07 cm^2), R_{CT} is the charge transfer resistance at the respective electrode, and C^0 is the concentration of the redox couple in the bulk solution (1 mM). The k_{et} of GCE, Co_3S_4, GCNNS, and Co_3S_4/GCNNS-modified composite electrodes were found to be 2.37×10^{-4}, 5.97×10^{-4}, 13.03×10^{-4}, and 26.71×10^{-4} cm^2 s^{-1}, respectively. The high k_{et} value achieved by Co_3S_4/GCNNS highlights the facile and faster electron transfer reaction at this electrode

surface than at Co_3S_4 or GCNNS. The results confirm that an efficient electrical network through Co_3S_4 anchored on the surface of GCNNS facilitates electron transfer in the composite-modified GCE. To further investigate the charge transfer, the photoluminescence (PL) of the materials was measured and is shown in Figure S2. At an excitation wavelength of 330 nm, both GCNNS and Co_3S_4/GCNNS show PL peaks around 450 nm. The GCNNS showed the highest PL intensity, indicating the faster recombination of photogenerated e- and h+ [38]. The decrease in PL intensity in the composite is due to the quenching of carrier recombination by Co_3S_4, and these electrons can be transferred at the interface. The results indicate that the heterogeneous electron transfer rate in Co_3S_4/GCNNS is larger than in GCNNS and is beneficial for H_2O_2 sensing.

3.3. Electrochemical Detection of H_2O_2
3.3.1. Electrochemical Reduction of H_2O_2 at Co_3S_4/GCNNS Modified GCE

The electrocatalytic properties of the fabricated electrodes towards H_2O_2 reduction were initially investigated using CV in a 0.2 M phosphate-buffered solution (PBS) of pH 7.2. Figure 8 shows the cyclic voltammograms obtained for bare and modified electrodes in the absence or presence of 1 mM H_2O_2, recorded between a potential range of 0.4 to -0.95 V at a scan rate of 50 mV/s. A bare GCE shows no redox features in the presence of H_2O_2 in Figure 8 (curve a). Figure 8 (curve b) shows that the GCE modified with GCNNS reduces H_2O_2 at a potential of -0.65 V to yield a peak current of -12.21 µA. The amino or cyano groups caused the activity on the surface of the GCNNS. The abundance of N atoms with lone pairs in their sp^2 orbitals in the GCNNS also aids in the adsorption of tiny molecules, such as H_2O_2 [27,32]. In this case, this favorable interaction between the analyte and the material facilitates electrocatalytic reduction. On the other hand, the electrochemical reduction of H_2O_2 at the Co_3S_4-modified GCE has the advantage of a lower reduction potential, as shown by Figure 8 (curve c). H_2O_2 is reduced at 200 mV less negative potential than the GCNNS electrode, but the peak current is less (-8.14 µA).
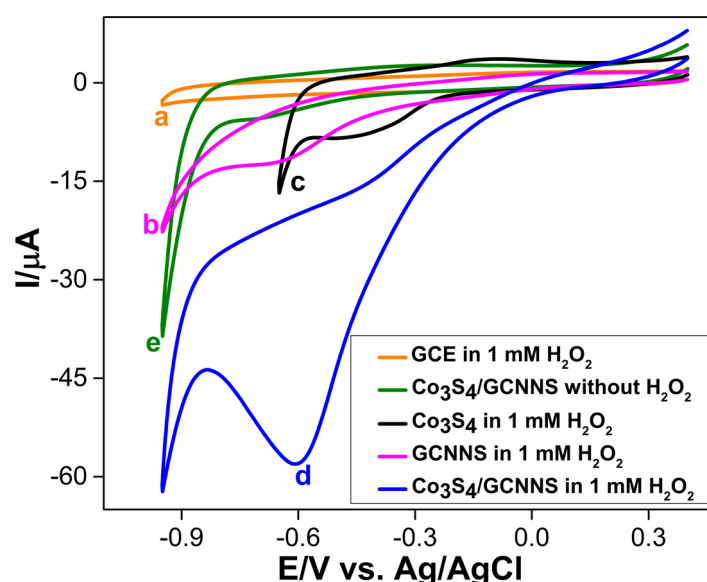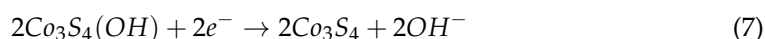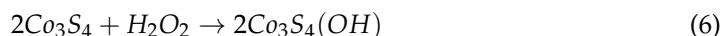

Figure 8. CVs obtained for the reduction of 1 mM H_2O_2 at (**a**) bare GCE, (**b**) GCNNS, (**c**) Co_3S_4, (**d**) Co_3S_4/GCNNS and (**e**) at Co_3S_4/GCNNS in the absence of H_2O_2, in 0.2 M PBS (pH 7.2) at a scan rate of 50 mV/s.

At the Co_3S_4/GCNNS electrode, a sharp and enhanced reduction peak can be observed at a potential of -0.6 V for the electroreduction of H_2O_2 in Figure 8 (curve d), while the electrode shows no response in the absence of H_2O_2, as seen in Figure 8 (curve e). The composite electrode delivers a large current of -58.2 µA, 4.7 times higher and 7.1 times higher than GCNNS and Co_3S_4-modified GCEs, respectively. Interestingly, the H_2O_2

reduction potential at Co_3S_4/GCNNS is reduced to 50 mV less negative than that at the GCNNS electrode. The cyclic voltammetric results show that the GCE modified with Co_3S_4/GCNNS shows the best performance towards H_2O_2 reduction.

The remarkable enhancement in the reduction peak currents can be attributed to the synergistic effect between Co_3S_4 and GCNNS that might have fastened the electron transfer with the H_2O_2 at the electrode surface. Co_3S_4 has good catalytic activity towards the reduction of H_2O_2 as it reduces the analyte at a lower potential. Still, the reduction peak current is lower, possibly due to the lower conductivity and small surface area of the Co_3S_4 micro flowers (0.097 cm^2). When combined with GCNNS, the effective surface area and conductivity are improved. As discussed earlier, the Co_3S_4/GCNNS electrode has a high electroactive surface area (0.18 cm^2), the lowest R_{CT} value (1.40 kΩ), indicating improved conductivity, and the highest charge transfer constant to facilitate faster electron transfer between the electrode and the analyte. These parameters are decisive in the superior electrocatalytic activity of the Co_3S_4/GCNNS electrode towards H_2O_2 reduction. All of these observations emphasize the excellent electrocatalytic activity of the Co_3S_4/GCNNS electrode.

The possible mechanism for the electroreduction of H_2O_2 at Co_3S_4/GCNNS can be expressed as in Equations (3)–(8). H_2O_2 reduction at the composite electrode occurs via the direct two-electron transfer pathway $\left(H_2O_2 + 2e^- \rightarrow 2OH^-\right)$ and is converted to H_2O. In the composite, both GCNNS and Co_3S_4 involve the reduction mechanism. The reaction at the GCNNS surface can be expressed as in Equations (3)–(5), where the active sites are the nitrogen-containing functional groups. While in Co_3S_4, H_2O_2 is reduced by the Co(II) ions and is converted to $Co_3S_4(OH)$. Co(III) in $Co_3S_4(OH)$ is again electro-reduced to Co(II), and Co_3S_4 is regenerated at the electrode surface. The corresponding mechanism is shown by Equations (6)–(8).

$$H_2O_2 + e^- \rightarrow OH_{ads} + OH^- \tag{3}$$

$$OH_{ads} + e^- \rightarrow OH^- \tag{4}$$

$$OH^- + H^+ \rightarrow H_2O \tag{5}$$

$$2Co_3S_4 + H_2O_2 \rightarrow 2Co_3S_4(OH) \tag{6}$$

$$2Co_3S_4(OH) + 2e^- \rightarrow 2Co_3S_4 + 2OH^- \tag{7}$$

$$OH^- + H^+ \rightarrow H_2O \tag{8}$$

As indicated by XPS, there is electron transfer between GCNNS and Co_3S_4, which could increase the active sites available for redox reactions. Additionally, the coordination bonds formed between the cobalt ion and the lone nitrogen pairs stabilize Co_3S_4 on the GCNNS surface, and since GCNNS readily adsorbs H_2O_2 on its surface, this also increases the interaction of H_2O_2 with Co(II) active sites and thereby favors a stronger reduction.

The response of Co_3S_4/GCNNS to 1 mM H_2O_2 was further studied by varying the scan rate from 10 to 60 mV/s, as shown in Figure 9a. Upon increasing the scan rates, the cathodic peak currents were increased. The peak current vs. scan rate was plotted, as shown in Figure 9b, and it showed a good linear relationship. The regression expression is I = $-0.66 \times \nu - 22.58$ with an R^2 value of 0.99. This indicates that the reduction of H_2O_2 at the Co_3S_4/GCNNS electrode is a surface adsorption-controlled process. The electrochemical reduction behavior of the composite electrode towards 1 mM H_2O_2 in different pH ranges from 3 to 11 was studied using CV in 0.2 M PBS at a scan rate of 50 mV/s. With an increase in the pH, the reduction peak potential of H_2O_2 on the composite electrode shifts to more negative values, as seen in Figure 9c. The shift in the peak potentials suggests that protons are involved in the electrochemical reduction. The reduction peak currents increase upon increasing the pH from 3 to 7 and decrease thereafter. The peak current achieves the maximum at a pH of 7; hence it is chosen for the electrochemical studies to determine H_2O_2. The relationship of reduction peak potential vs. pH is plotted in Figure 9d, showing a linear relationship. The regression equation is E = $-0.05 \times$ pH $- 0.28$ with an R^2 value of 0.99.

The slope of the curve is around 59 mV, which matches the theoretical value for the two protons and two electrons reaction.
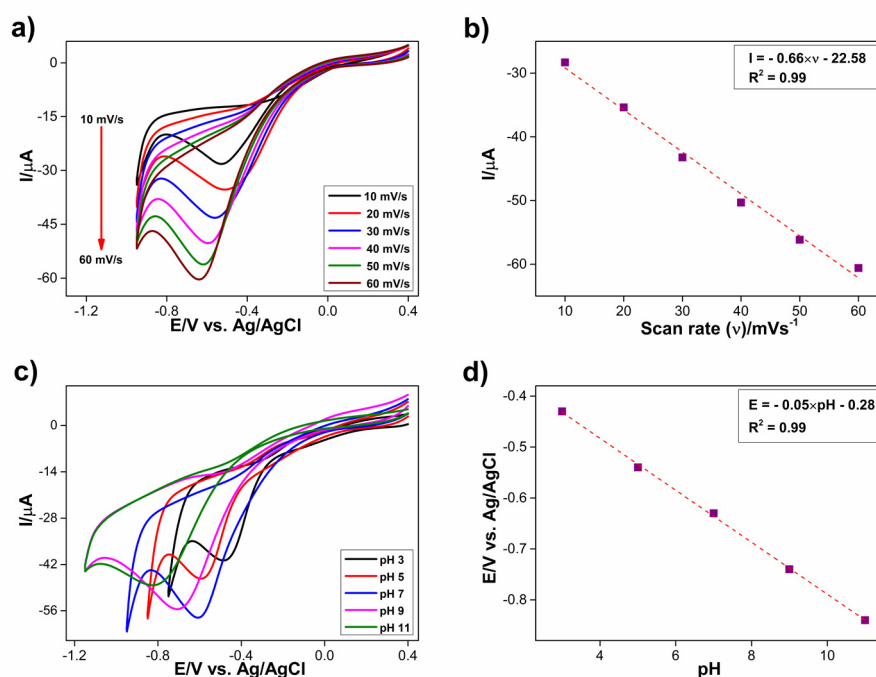

Figure 9. (**a**) CVs obtained for the reduction of 1 mM H_2O_2 at Co_3S_4/GCNNS in 0.2 M PBS at different scan rates from 10–60 mV s^{-1}, (**b**) calibration plot of peak current with respect to the scan rate, (**c**) CVs obtained for the reduction of 1 mM H_2O_2 at the Co_3S_4/GCNNS electrode at different pH of 3, 5, 7, 9, and 11 in 0.2 M PBS at a scan rate of 50 mV/s, (**d**) plot of the reduction potential of H_2O_2 vs. pH of the PBS.

The loading levels of Co_3S_4 and GCNNS were varied to optimize the performance of the composite electrode. First, the concentrations of Co_3S_4 varied between 0.1, 0.15, 0.2, and 0.25 mg in 1 mg/mL GCNNS. The cyclic voltammograms recorded for 1 mM H_2O_2 are shown in Figure S3a, in which the peak current increases up to a load of 0.2 mg; beyond that, the current decreases, and the shape of the CV curve changes as the capacitance current and onset potential increase. This is possible because above 0.2 mg, Co_3S_4 agglomerates on the GCNNS surface, reducing the number of catalytically active sites available for H_2O_2 reduction.

Furthermore, the weight of GCNNS was varied to 0.5, 1, and 1.5 mg for a weight of Co_3S_4 of 0.2 mg/mL water, and the recorded CV curves are shown in Figure S3b. At a loading of 0.5 mg/mL, the peak reduction current is lower; with an increase in the GCNNS level, there is an increase in peak current, but above 1 mg/mL, the activity decreases. This is due to the agglomeration of the nanosheets and the loss of active sites on the electrode surface due to the increased loading. Therefore, the optimal combination to produce the best-performing Co_3S_4/GCNNS composite electrode was determined to be 0.2 mg Co_3S_4 and 1 mg GCNNS in 1 mL distilled water, which was then used for subsequent electrochemical studies.

3.3.2. Sensitive Determination of H_2O_2

As illustrated in Figure 10a, differential pulse voltammetry (DPV) was achieved for the successive injection of 1 μM of H_2O_2 in 0.2 M PBS (pH 7.2) at the Co_3S_4/GCNNS electrode. The reduction current rose linearly with each addition of H_2O_2. Still, the reduction potential remained constant at −0.52 V. This suggests that it is possible to sensitively measure H_2O_2 at Co_3S_4/GCNNS without impacting its reduction potential. The regression relation I = −0.05 × c − 1.24 represents the calibration plot between the reduction current and

concentration of H_2O_2 in Figure 10b, and it displays a strong linear relationship with an R^2 value of 0.99.
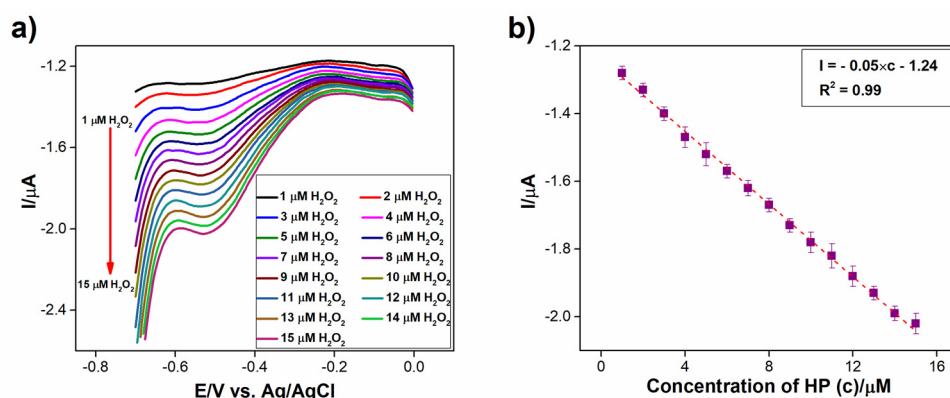

Figure 10. (**a**) DPVs obtained for the reduction of 1 μM of H_2O_2 at Co_3S_4/GCNNS modified GCE electrode in 0.2 M PBS of pH 7.2, (**b**) calibration plot of peak current against the concentration of H_2O_2.

3.3.3. Amperometric Sensing of H_2O_2 at Co_3S_4/GCNNS Modified GCE

Wide-range amperometry was employed to evaluate the application of the Co_3S_4/GCNNS electrode in the detection of H_2O_2, as depicted in Figure 11a. The amperometric i–t curve was obtained at a constant potential of −0.7 V, and the concentration of H_2O_2 varied from 10 nM to 1.5 mM in 0.2 M PBS of pH 7.2. During each addition of H_2O_2, a well-defined increase in the current was observed. The sharp increase in the current is due to the electroreduction of H_2O_2 at the Co_3S_4/GCNNS electrode. A steady state of the final reduction current was reached in 3 s, indicating the rapid response of the electrode to H_2O_2. The amperometric response also demonstrates the excellent electrocatalytic performance of the Co_3S_4/GCNNS composite electrode. The linear increase in the reduction current with the increasing H_2O_2 concentration validates its practical application as an H_2O_2 sensor. As shown in Figure 11b, the calibration curve for the sensor was plotted between the H_2O_2 concentrations and the reduction currents obtained. The regression equation for the calibration curve is obtained as $I = -0.08 \times c - 2.02$ showing good linearity with an R^2 value of 0.99. The limit of detection of the sensor was calculated to be 70 nM (S/N = 3), and it shows a sensitivity of 1.16 $\mu A \mu M^{-1} cm^{-2}$ (slope/area). The analytical performance of Co_3S_4/GCNNS is compared to various non-enzymatic sensors in Table S2. Shu et al. developed a TiO_2/SiO_2 composite as a phosphorescence sensor for H_2O_2 [47]. Although it detects H_2O_2 over a wide range of analyte concentrations, the LOD is as low as 0.16 μM. The graphene-CdS electroluminescence sensor detects H_2O_2 in a range from 5 μM to 1 mM but has a low LOD of 1.7 μM [48]. Gan et al. explored MoS_2 quantum dots as a fluorescence sensor and determined H_2O_2 in a narrow range of 2–20 μM [49]. Calorimetric detection of H_2O_2 has been demonstrated by porphyrin iron-grafted mesoporous silica composites, but the detection limit is low as 67 μM [50]. Ding et al. presented an optical sensor for H_2O_2 in the 1 μM to 10 mM range by growing Pt nanoparticles inside the pores of fibrous silica particles and with a low LOD of 15 μM [51]. Co_3S_4/GCNNS has a very high LOD and sensitivity than these sensors. Further, the performance of Co_3S_4/GCNNS is compared with related electrochemical sensors (Table S2). Co_3O_4 hollow-sphere-based H_2O_2 sensor has low LOD and sensitivity compared to Co_3S_4/GCNNS [52]. Au/Cu bimetallic nanoparticles reported by Gowthaman et al. are expensive and have low LOD and sensitivity [53]. Chen et al. presented Cu_2S@Co_3S_4 for the excellent electrocatalytic reduction of H_2O_2 using CV but did not explore the sensor aspects in detail [24]. GCN hollow spheres operate in a short range and have low sensitivity and LOD [27]. Liu et al. synthesized ZnO/GCNNS for H_2O_2 oxidation, but the sensor has a low LOD [31]. Atacan et al. prepared CuO/GCN nanoflakes. They demonstrated the sensing of H_2O_2 using DPV with high sensitivity, but the operation is limited to a short range, and the LOD is in the

micromolar range. Recently, Ye et al. reported $ZnFe_2O_4$/GCN nano-micro composite for H_2O_2 sensing but has a very low sensitivity and LOD compared to Co_3S_4/GCNNS [3]. It is visible that Co_3S_4/GCNNS is an improvement over these proposed H_2O_2 sensors.
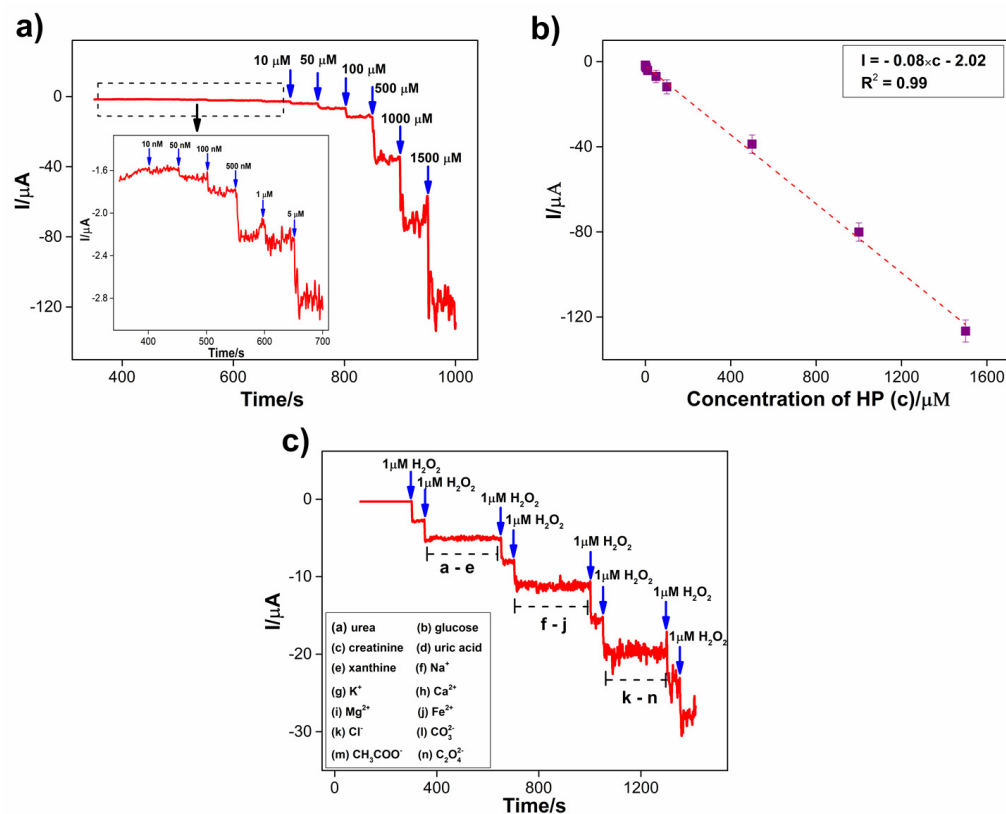

Figure 11. Amperometric i-t curve obtained for the reduction of H_2O_2 at Co_3S_4/GCNNS in 0.2 M PBS (pH 7.2) at an applied potential of -0.7 V for (**a**) an addition of H_2O_2 of concentration from 10 nM to 1.5 mM, (**b**) calibration plot of current vs. concentration of H_2O_2, (**c**) for the reduction of 1 μM H_2O_2 in presence of 500 μM of potential interferences.

One of the most common problems when using sensors to determine H_2O_2 in real samples is their response to the interfering species. To investigate the selectivity of Co_3S_4/GCNNS towards H_2O_2 detection, the influence of other common components in blood serum was examined by amperometry at -0.7 V in 0.2 M PBS of pH 7.2. It is reported that the H_2O_2 concentration present in human blood serum is generally less than 10 μM. In contrast, creatinine and xanthine are present in blood serum at concentrations below 119.3 μM and 2 mM, respectively. For non-diabetics, the normal glucose level is between 3.9 and 7.1 mM. The uric acid concentration ranges from 208 to 428 μM, and the urea concentration ranges between 2.5 and 7.5 mM [54–57]. On average, these species are present at less than or around 500 times the serum H_2O_2 concentration. Therefore, 500-fold concentrations of these potential interferences are chosen to study the selectivity of Co_3S_4/GCNNS towards the electroreduction of 1 μM H_2O_2. As shown in Figure 11c, after attaining a stable response in PBS, 1 μM H_2O_2 was added to the PBS, and the corresponding increase in the reduction current indicated the proper functioning of the Co_3S_4/GCNNS electrode. Then, 1 μM H_2O_2 was added in another step to obtain the same increase in reduction current as in the previous step. Further, every 60 s, 500 μM of urea, glucose, creatinine, uric acid, and xanthine were added, respectively, to the region marked as a–e (Figure 11c). As shown, no appreciable increase in the current was observed upon their addition, confirming that they show no interference at the Co_3S_4/GCNNS electrode. The amperometric current at the modified electrode increases for two consecutive additions of 1 μM of H_2O_2, indicating that the previously added species has no effect on the reduction

of H_2O_2 at Co_3S_4/GCNNS. Furthermore, the influence of the common cations present in the blood serum was studied by adding 500 µM of salts of each Na^+, K^+, Ca^{2+}, Mg^{2+}, and Fe^{2+}, respectively (f–j); nevertheless, no change in current was observed, still a spike of 1 µM of H_2O_2 increases the current response indicating the selectivity of Co_3S_4/GCNNS electrode towards H_2O_2 than to these cations. Further 500 µM concentrations of anions, Cl^-, CO_3^{2-}, CH_3COO^-, and $C_2O_4^{2-}$ were each added at 60 s intervals, as shown in the region; k–n, and only a negligible change in current was observed, whereas two successive additions of H_2O_2 resulted in the increase of current due to the reduction of H_2O_2. The results confirm that 500-fold additions of these entities do not alter the current response due to H_2O_2 reduction, proving the high selectivity of the Co_3S_4/GCNNS electrode as an H_2O_2 sensor.

3.3.4. Stability of Co_3S_4/GCNNS Modified GCE Sensor

Cyclic voltammetric responses of Co_3S_4/GCNNS-modified GCE towards 1 mM of H_2O_2 in 0.2 M PBS (pH = 7.2) were obtained for many 1, 2, 3, 4, 5, 6, and 10 days to confirm the long-term stability and repeatability of the proposed sensor, and the recorded cyclic voltammograms are shown in Figure 12a. The H_2O_2 reduction current showed no noticeable change, and the reduction potential remained unaltered, indicating the good stability of the fabricated sensor toward H_2O_2 reduction. Furthermore, the amperometric i–t curve of the Co_3S_4/GCNNS electrode was recorded for 4000 s at an applied potential of -0.7 V in 0.2 M PBS (pH 7.2) and is shown in Figure 12b. The current response was constant throughout the experiment, showing good amperometric stability of the Co_3S_4/GCNNS electrode in PBS.
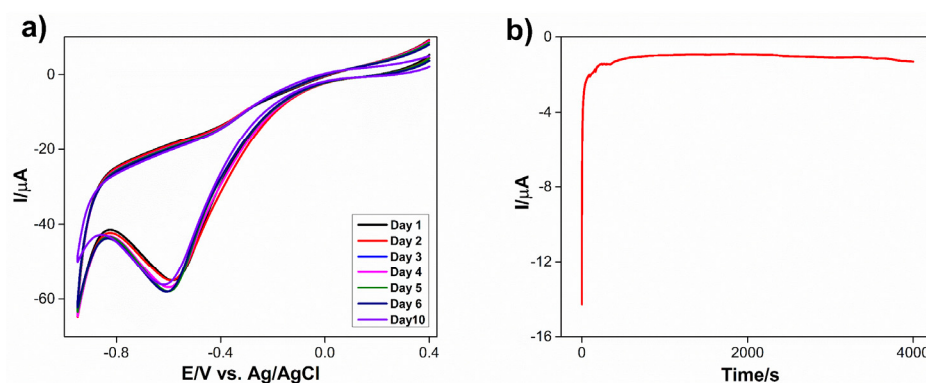

Figure 12. (**a**) CVs obtained for the reduction of 1 mM of H_2O_2 at Co_3S_4/GCNNS modified GCE in 0.2 M PBS for days from 1 to 10, (**b**) amperometric i–t curve obtained for Co_3S_4/GCNNS modified GCE for 4000s at an applied potential of -0.7 V in 0.2 M PBS pH 7.2.

3.3.5. Real Sample Analysis

The determination of H_2O_2 in human blood serum was performed at the Co_3S_4/GCNNS electrode using DPV in 0.2 M PBS of pH 7.2 to check the practical applicability of the proposed sensor, which is shown in Figure 13 (curve a). The reduction peak for H_2O_2 in the serum sample appears around -0.52 V. The H_2O_2 concentration in the serum was found to be 3.2 µM, which is within the normal range. An additional 50 µM of H_2O_2 was added to the serum, and the reduction peak current increased without affecting the reduction potential, as shown in Figure 13 (curve b). A recovery of 98.5 % was achieved. This indicates that the proposed sensor can be employed for monitoring H_2O_2 in real samples.
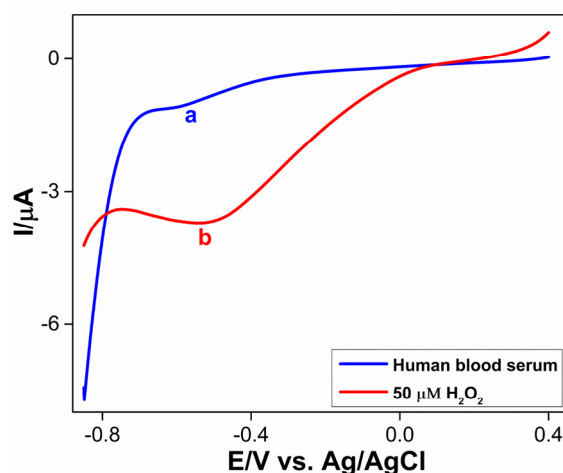
Figure 13. DPVs obtained for (**a**) human blood serum and (**b**) addition of 50 μM H_2O_2 at Co_3S_4/GCNNS modified GCE in serum.

4. Conclusions

Co_3S_4/GCNNS were synthesized as a promising material for the electrocatalytic reduction of H_2O_2 by a simple and low-cost method. Physical and chemical characterizations helped us to confirm the successful formation of the materials. Nanosheets of GCNNS and micro flowers of Co_3S_4 were observed by SEM. From CV, the Co_3S_4/GCNNS composite was observed to reduce H_2O_2 and provide 4.7 and 7.1 times higher reduction current compared to pure Co_3S_4 and GCNNS, respectively, showing excellent electrocatalytic activity. The hybridization between Co_3S_4 and GCNNS enhanced the electroactive surface area and conductivity of the proposed sensor, which are crucial for superior electrocatalytic activity. At the same time, as evident from XPS studies, the electronic interactions between GCNNS and Co_3S_4 enhance the catalytically active redox centers on the Co_3S_4/GCNNS surface for H_2O_2 reduction. Co_3S_4/GCNNS was further explored for the amperometric sensing of H_2O_2 to show high performance over a wide range from 10 nM to 1.5 mM with a high detection limit of 70 nM. The sensor showed a fast response and excellent selectivity against potential interferences, and the practicality of the sensor was evaluated by the determination of H_2O_2 in the human serum. The current work demonstrates the potential of Co_3S_4/GCNNS as an ideal material for constructing high-performance H_2O_2 sensors.

Supplementary Materials: The following supporting information can be downloaded at: https://www.mdpi.com/article/10.3390/bios13010108/s1, Details on materials, characterization, and electrochemical studies are provided. Figure S1: XPS spectra of GCNNS, (a) survey scan, high-resolution spectra of (b) C 1s and (c) N1s. XPS spectra of Co_3S_4, (d) survey scan, high-resolution spectra of (e) Co 2p and (f) S 2p., Figure S2: Comparison of PL spectra of Co_3S_4, GCNNS, and Co_3S_4/GCNNS measured at an excitation wavelength of 330 nm., Figure S3: (a) CVs obtained for the reduction of 1 mM H_2O_2 at 1 mg/mL GCNNS containing various amounts of Co_3S_4; 0.1, 0.15, 0.2, and 0.25 mg/mL in 0.2 M PBS pH 7.2, (b) CVs obtained for the reduction of 1 mM H_2O_2 at 0.2 mg/mL Co_3S_4 containing various amount of GCNNS of 0.5, 1 and 1.5 mg/mL. Table S1: Comparison of the binding energy of the core levels in Co_3S_4, GCN, and Co_3S_4/GCNNS. Table S2: Comparison of related non-enzymatic electrochemical sensors for H_2O_2 sensors with the performance of Co_3S_4/GCNNS.

Author Contributions: Conceptualization, A.R., A.A., N.S.G., S.R.K.V., S.A.J. and C.S.; Methodology, A.R., A.A. and N.S.G.; Investigation, A.R. and A.A.; Resources, S.A.J. and C.S.; Writing—original draft, A.R.; Writing—review and editing, A.R., A.A., N.S.G., S.R.K.V., S.A.J., V.B. and C.S.; Visualization, A.R.; Critical thinking, V.B.; Supervision, S.R.K.V. and C.S. All authors have read and agreed to the published version of the manuscript.

References

1. Dai, H.; Chen, Y.; Niu, X.; Pan, C.; Chen, H.; Chen, X. High-performance electrochemical biosensor for nonenzymatic H_2O_2 sensing based on Au@C-Co_3O_4 heterostructures. *Biosens. Bioelectron.* **2018**, *118*, 36–43. [CrossRef] [PubMed]

2. Kubendhiran, S.; Thirumalraj, B.; Chen, S.-M.; Karuppiah, C. Electrochemical co-preparation of cobalt sulfide/reduced graphene oxide composite for electrocatalytic activity and determination of H_2O_2 in biological samples. *J. Colloid Interface Sci.* **2018**, *509*, 153–162. [CrossRef]

3. Ye, M.; Yang, C.; Sun, Y.; Wang, J.; Wang, D.; Zhao, Y.; Zhu, Z.; Liu, P.; Zhu, J.; Li, C.; et al. $ZnFe_2O_4$/Graphitic Carbon Nitride Nano/Microcomposites for the Enhanced Electrochemical Sensing of H_2O_2. *ACS Appl. Nano Mater.* **2022**, *5*, 10922–10932. [CrossRef]

4. Wu, J.; Wu, Y.; Lu, L.; Zhang, D.; Wang, X. Single-atom Au catalyst loaded on CeO_2: A novel single-atom nanozyme electrochemical H_2O_2 sensor. *Talanta Open* **2021**, *4*, 100075. [CrossRef]

5. Shi, L.; Layani, M.; Cai, X.; Zhao, H.; Magdassi, S.; Lan, M. An inkjet printed Ag electrode fabricated on plastic substrate with a chemical sintering approach for the electrochemical sensing of hydrogen peroxide. *Sens. Actuators B Chem.* **2018**, *256*, 938–945. [CrossRef]

6. Liu, Y.; Li, H.; Gong, S.; Chen, Y.; Xie, R.; Wu, Q.; Tao, J.; Meng, F.; Zhao, P. A novel non-enzymatic electrochemical biosensor based on the nanohybrid of bimetallic PdCu nanoparticles/carbon black for highly sensitive detection of H_2O_2 released from living cells. *Sens. Actuators B Chem.* **2019**, *290*, 249–257. [CrossRef]

7. Klassen, N.; Marchington, D.; McGowan, H. H_2O_2 Determination by the I3- Method and by $KMnO_4$ Titration. *Anal. Chem.* **1994**, *66*, 2921–2925. [CrossRef]

8. Ye, S.; Hananya, N.; Green, O.; Chen, H.; Zhao, A.; Shen, J.; Shabat, D.; Yang, D. A Highly Selective and Sensitive Chemiluminescent Probe for Real-Time Monitoring of Hydrogen Peroxide in Cells and Animals. *Angew. Chem. Int. Ed.* **2020**, *59*, 14326–14330. [CrossRef]

9. Khan, S.; Jin, E.; Sojic, N.; Pantano, P. A fluorescence-based imaging-fiber electrode chemical sensor for hydrogen peroxide. *Anal. Chim. Acta* **2000**, *404*, 213–221. [CrossRef]

10. Beers, R.; Sizer, I. A spectrophotometric method for measuring the breakdown of hydrogen peroxide by catalase. *J. Biol. Chem.* **1952**, *195*, 133–140. [CrossRef]

11. Karuppiah, C.; Venkatesh, K.; Arunachalam, P.; Ramaraj, S.; Al-Mayouf, A.; Yang, C.-C. Optimization of S-dopant on N, S co-doped graphene/CNT-Fe_3C nanocomposite electrode for non-enzymatic H_2O_2 sensor. *Mater. Lett.* **2021**, *285*, 129001. [CrossRef]

12. Zhu, C.; Yang, G.; Li, H.; Du, D.; Lin, Y. Electrochemical Sensors and Biosensors Based on Nanomaterials and Nanostructures. *Anal. Chem.* **2015**, *87*, 230–249. [CrossRef] [PubMed]

13. Liu, H.; Weng, L.; Yang, C. A review on nanomaterial-based electrochemical sensors for H_2O_2, H_2S and NO inside cells or released by cells. *Microchim. Acta* **2017**, *184*, 1267–1283. [CrossRef]

14. Cao, D.; Chao, J.; Sun, L.; Wang, G. Catalytic behavior of Co_3O_4 in electroreduction of H_2O_2. *J. Power Sources* **2008**, *179*, 87–91. [CrossRef]

15. Salimi, A.; Hallaj, R.; Soltanian, S.; Mamkhezri, H. Nanomolar detection of hydrogen peroxide on glassy carbon electrode modified with electrodeposited cobalt oxide nanoparticles. *Anal. Chim. Acta* **2007**, *594*, 24–31. [CrossRef]

16. Li, S.-J.; Du, J.-M.; Zhang, J.-P.; Zhang, M.-J.; Chen, J. A glassy carbon electrode modified with a film composed of cobalt oxide nanoparticles and graphene for electrochemical sensing of H_2O_2. *Microchim. Acta* **2014**, *181*, 631–638. [CrossRef]

17. Ullah, R.; Rasheed, M.; Abbas, S.; Rehman, K.; Shah, A.; Ullah, K.; Khan, Y.; Bibi, M.; Ahmad, M.; Ali, G. Electrochemical sensing of H_2O_2 using cobalt oxide modified TiO_2 nanotubes. *Curr. Appl. Phys.* **2022**, *38*, 40–48. [CrossRef]

18. Liu, T.; Zhang, X.; Fu, K.; Zhou, N.; Xiong, J.; Su, Z. Fabrication of Co_3O_4/$NiCo_2O_4$ Nanocomposite for Detection of H_2O_2 and Dopamine. *Biosensors* **2021**, *11*, 452. [CrossRef]

19. Wang, H.; Shu, T.; Lin, C.; Sun, F.; Wang, Z.; Lin, B.; Wei, F.; Yao, K.X.; Qi, J.; Sui, Y. Hierarchical construction of Co_3S_4 nanosheet coated by 2D multi-layer MoS_2 as an electrode for high performance supercapacitor. *Appl. Surf. Sci.* **2022**, *578*, 151897. [CrossRef]

20. Xue, Z.; Lv, L.; Tian, Y.; Tan, S.; Ma, Q.; Tao, K.; Han, L. Co_3S_4 Nanoplate Arrays Decorated with Oxygen-Deficient CeO_2 Nanoparticles for Supercapacitor Applications. *ACS Appl. Nano Mater.* **2021**, *4*, 3033–3043. [CrossRef]

21. Ji, Z.; Li, N.; Xie, M.; Shen, X.; Dai, W.; Liu, K.; Xu, K.; Zhu, G. High-performance hybrid supercapacitor realized by nitrogen-doped carbon dots modified cobalt sulfide and reduced graphene oxide. *Electrochim. Acta* **2020**, *334*, 135632. [CrossRef]

22. Yang, Z.; Bai, X.; Zhu, S.; Qi, C. Synthesis of porous Co_3S_4 for enhanced voltammetric nonenzymatic determination of glucose. *Microchim. Acta* **2020**, *187*, 98. [CrossRef]

23. Huang, D.; Yang, L.; Li, X.; Zou, L.; Ye, B. A new electrochemical sensor for Taxifolin based on RGO-Co_3S_4@MoS_2 modified electrode. *J. Electroanal. Chem.* **2019**, *851*, 113473. [CrossRef]

24. Chen, H.; Cai, J.; Yang, J.; Zhong, Z.; Ma, M.; Deng, W.; Tan, Y.; Xie, Q. Synergistic electrocatalysis of Cu_2S@Co_3S_4 core-shell heterostructures toward H_2O_2 reduction and their application for sensitive immunosensing of alpha fetoprotein. *Sens. Actuators B Chem.* **2021**, *348*, 130703. [CrossRef]

25. Huang, H.-Q.; Li, Y.-Y.; Chen, S.-H.; Liu, Z.-G.; Cui, Y.-M.; Li, H.-Q.; Guo, Z.; Huang, X.-J. Noble-metal-free Fe_3O_4/Co_3S_4 nanosheets with oxygen vacancies as an efficient electrocatalyst for highly sensitive electrochemical detection of As(III). *Anal. Chim. Acta* **2022**, *1189*, 339208. [CrossRef] [PubMed]

26. Idris, A.; Oseghe, E.; Msagati, T.; Kuvarega, A.; Feleni, U.; Mamba, B. Graphitic Carbon Nitride: A Highly Electroactive Nanomaterial for Environmental and Clinical Sensing. *Sensors* **2020**, *20*, 5743. [CrossRef]

27. Puentes-Prado, E.; Gutiérrez-Granados, S.; Gómez-Solís, C.; Ramírez-García, G. Enhanced photo-electrochemical response of screen-printed electrodes based on g-C_3N_4 hollow spheres and other morphologies for sensing applications. *FlatChem* **2022**, *35*, 100412. [CrossRef]

28. Ahmad, K.; Kim, H. Design and preparation of g-C_3N_4/rGO modified screen printed electrode for hydrogen peroxide sensing application. *Synth. Met.* **2022**, *286*, 117047. [CrossRef]

29. Luo, Y.; Yan, Y.; Zheng, S.; Xue, H.; Pang, H. Graphitic carbon nitride based materials for electrochemical energy storage. *J. Mater. Chem. A Mater.* **2019**, *7*, 901–924. [CrossRef]

30. Ajith, A.; John, S. Performance of graphitic carbon nitride nanosheets derived from liquid and thermal exfoliations towards the electrochemical reduction of nitrobenzene. *New J. Chem.* **2022**, *46*, 6446–6452. [CrossRef]

31. Liu, H.; Zhang, Y.; Dong, Y.; Chu, X. Synthesis of ZnO/g-C_3N_4 Nanocomposite and Its Electrochemical Application in Hydrogen Peroxide Detection. *Russ. J. Electrochem.* **2021**, *57*, 808–815. [CrossRef]

32. Atacan, K.; Özacar, M. Construction of a non-enzymatic electrochemical sensor based on CuO/g-C_3N_4 composite for selective detection of hydrogen peroxide. *Mater. Chem. Phys.* **2021**, *266*, 124527. [CrossRef]

33. Chauhan, M.; Reddy, K.; Gopinath, C.; Deka, S. Copper Cobalt Sulfide Nanosheets Realizing a Promising Electrocatalytic Oxygen Evolution Reaction. *ACS Catal.* **2017**, *7*, 5871–5879. [CrossRef]

34. Seredych, M.; Łoś, S.; Giannakoudakis, D.; Rodríguez-Castellón, E.; Bandosz, T. Photoactivity of g-C_3N_4 /S-Doped Porous Carbon Composite: Synergistic Effect of Composite Formation. *ChemSusChem* **2016**, *9*, 795–799. [CrossRef]

35. Wang, Y.; Hao, X.; Zhang, L.; Jin, Z.; Zhao, T. Amorphous Co_3S_4 nanoparticle-modified tubular g-C_3N_4 forms step-scheme heterojunctions for photocatalytic hydrogen production. *Catal. Sci. Technol.* **2021**, *11*, 943–955. [CrossRef]

36. Ramesh, A.; Gavaskar, D.; Nagaraju, P.; Duvvuri, S.; Vanjari, S.; Subrahmanyam, C. Mn-doped ZnO microspheres prepared by solution combustion synthesis for room temperature NH_3 sensing. *Appl. Surf. Sci. Adv.* **2022**, *12*, 100349. [CrossRef]

37. Gan, Z.; Shan, Y.; Chen, J.; Gui, Q.; Zhang, Q.; Nie, S.; Wu, X. The origins of the broadband photoluminescence from carbon nitrides and applications to white light emitting. *Nano Res.* **2016**, *9*, 1801–1812. [CrossRef]

38. Shan, Y.; Wang, Y.; Shi, C.; Gan, Z. Relaxation of Excited Electrons on Carbon Nitrides Investigated by Electrochemiluminescence and Photoluminescence Spectra. *J. Phys. Chem. C* **2020**, *124*, 19314–19323. [CrossRef]

39. Liang, Z.; Xue, Y.; Wang, X.; Zhang, X.; Tian, J.; Cui, H. The incorporation of cocatalyst cobalt sulfide into graphitic carbon nitride: Boosted photocatalytic hydrogen evolution performance and mechanism exploration. *Nano Mater. Sci.* **2022**; *in press*. [CrossRef]

40. Li, X.; Zhang, J.; Shen, L.; Ma, Y.; Lei, W.; Cui, Q.; Zou, G. Preparation and characterization of graphitic carbon nitride through pyrolysis of melamine. *Appl. Phys. A* **2009**, *94*, 387–392. [CrossRef]

41. Yang, H.; Yin, J.; Cao, R.; Sun, P.; Zhang, S.; Xu, X. Constructing highly dispersed 0D Co_3S_4 quantum dots/2D g-C_3N_4 nanosheets nanocomposites for excellent photocatalytic performance. *Sci. Bull.* **2019**, *64*, 1510–1517. [CrossRef]

42. Li, W.; Li, Y.; Yang, C.; Ma, Q.; Tao, K.; Han, L. Fabrication of 2D/2D nanosheet heterostructures of ZIF-derived Co_3S_4 and g-C_3N_4 for asymmetric supercapacitors with superior cycling stability. *Dalton Trans.* **2020**, *49*, 14017–14029. [CrossRef] [PubMed]

43. Li, Y.; Xu, J.; Liu, Z.; Yu, H. Synthesis of $Ni_{12}P_5$ on Co_3S_4 material for effectively improved photocatalytic hydrogen production from water splitting under visible light. *J. Mater. Sci. Mater. Electron.* **2019**, *30*, 11694–11705. [CrossRef]

44. Ye, L.; Fu, J.; Xu, Z.; Yuan, R.; Li, Z. Facile One-Pot Solvothermal Method to Synthesize Sheet-on-Sheet Reduced Graphene Oxide (RGO)/$ZnIn_2S_4$ Nanocomposites with Superior Photocatalytic Performance. *ACS Appl. Mater. Interfaces* **2014**, *6*, 3483–3490. [CrossRef] [PubMed]

45. Jafarian, M.; Mahjani, M.; Heli, H.; Gobal, F.; Khajehsharifi, H.; Hamedi, M. A study of the electro-catalytic oxidation of methanol on a cobalt hydroxide modified glassy carbon electrode. *Electrochim. Acta* **2003**, *48*, 3423–3429. [CrossRef]

46. Yang, Z.; Chen, C.-Y.; Chang, H.-T. Supercapacitors incorporating hollow cobalt sulfide hexagonal nanosheets. *J. Power Sources* **2011**, *196*, 7874–7877. [CrossRef]

47. Shu, X.; Chen, Y.; Yuan, H.; Gao, S.; Xiao, D. H_2O_2 Sensor Based on the Room-Temperature Phosphorescence of Nano TiO_2 /SiO_2 Composite. *Anal. Chem.* **2007**, *79*, 3695–3702. [CrossRef]

48. Wang, K.; Liu, Q.; Wu, X.-Y.; Guan, Q.-M.; Li, H.-N. Graphene enhanced electrochemiluminescence of CdS nanocrystal for H_2O_2 sensing. *Talanta* **2010**, *82*, 372–376. [CrossRef]

49. Gan, Z.; Gui, Q.; Shan, Y.; Pan, P.; Zhang, N.; Zhang, L. Photoluminescence of MoS_2 quantum dots quenched by hydrogen peroxide: A fluorescent sensor for hydrogen peroxide. *J. Appl. Phys.* **2016**, *120*, 104503. [CrossRef]

50. Zhu, P.; Xu, Z.; Cai, L.; Chen, J. Porphyrin Iron-Grafted Mesoporous Silica Composites for Drug Delivery, Dye Degradation and Colorimetric Detection of Hydrogen Peroxide. *Nanoscale Res. Lett.* **2021**, *16*, 41. [CrossRef]

51. Ding, L.; Chen, S.; Zhang, W.; Zhang, Y.; Wang, X. Fully Reversible Optical Sensor for Hydrogen Peroxide with Fast Response. *Anal. Chem.* **2018**, *90*, 7544–7551. [CrossRef]

52. Wang, M.; Jiang, X.; Liu, J.; Guo, H.; Liu, C. Highly sensitive H_2O_2 sensor based on Co_3O_4 hollow sphere prepared via a template-free method. *Electrochim. Acta* **2015**, *182*, 613–620. [CrossRef]

53. Gowthaman, N.; Shankar, S.; John, S.A. Substrate catalyzed formation of Au-Cu bimetallic nanoparticles as electrocatalyst for the reduction of dioxygen and hydrogen peroxide. *J. Electroanal. Chem.* **2018**, *812*, 37–44. [CrossRef]

54. Gaikwad, R.; Thangaraj, P.; Sen, A. Direct and rapid measurement of hydrogen peroxide in human blood using a microfluidic device. *Sci. Rep.* **2021**, *11*, 2960. [CrossRef] [PubMed]

55. Forman, H.; Bernardo, A.; Davies, K. What is the concentration of hydrogen peroxide in blood and plasma? *Arch. Biochem. Biophys.* **2016**, *603*, 48–53. [CrossRef] [PubMed]

56. Hira, H.; Samal, P.; Kaur, A.; Kapoor, S. Plasma level of hypoxanthine/xanthine as markers of oxidative stress with different stages of obstructive sleep apnea syndrome. *Ann. Saudi Med.* **2014**, *34*, 308–313. [CrossRef] [PubMed]

57. Chou, J.-C.; Wu, C.-Y.; Lin, S.-H.; Kuo, P.-Y.; Lai, C.-H.; Nien, Y.-H.; Wu, Y.-X.; Lai, T.-Y. The Analysis of the Urea Biosensors Using Different Sensing Matrices via Wireless Measurement System & Microfluidic Measurement System. *Sensors* **2019**, *19*, 3004. [CrossRef] [PubMed]